

A two dimensional vision-based force sensor for microrobotic applications

David J. Cappelleri^{a,*}, Gianluca Piazza^b, Vijay Kumar^a

^a GRASP Lab, Department of Mechanical Engineering and Applied Mechanics, University of Pennsylvania, Philadelphia, PA, USA

^b Department of Electrical and Systems Engineering, University of Pennsylvania, Philadelphia, PA, USA

ARTICLE INFO

Article history:

Received 3 June 2009

Received in revised form 25 June 2010

Accepted 18 June 2011

Available online 29 June 2011

Keywords:

Vision-based sensor

Micro-Newton force sensing

PDMS compliant mechanism

Microrobotics

ABSTRACT

We present a two-dimensional, vision-based force sensor, capable of sensing micro-Newton level forces for use in microrobotic applications. Our design consists of a planar, elastic mechanism with known force-deflection characteristics. A CCD camera attached to an optical microscope is used to track the deformation of the mechanism as it is used to manipulate objects in a microrobotic test-bed. By observing the displacements of select points in the mechanism, the manipulation forces can be extracted in real-time to achieve force-guided manipulation of micro-scale objects. The modeling, design, microfabrication, calibration and experimental validation of the force sensor for use in a microassembly application are presented here along with preliminary results for next generation designs.

© 2011 Elsevier B.V. All rights reserved.

1. Introduction

The real advantages of a high precision microrobot or manipulation system can only be utilized if the automated system also has high resolution sensors along with good control strategies [1]. Force sensors capable of resolving micro-Newton (μN) level forces, the typical forces encountered when manipulating biological cells and micro- and meso-scale parts, are generally made using microfabrication techniques. However, indirect force measurements, like mounting strain gauges [2–5], capacitance-based force measurement [6–10], or piezoresistive cantilever force measurement [11], are difficult to implement at the MEMS scale because they substantially complicate the microfabrication process and drive up production cost. Indeed, there are no commercially available, inexpensive, multi-axis force sensors at this scale that can be easily integrated with microrobotic manipulators. Our goal is to come up with a design that can be easily integrated into a microrobotic test-bed (Fig. 1(left) [12,13]), which does not require any alteration of the object being manipulated or require exotic fabrication techniques or drive electronics and can sense μN level forces in two dimensions. With such a design, real-time controlled manipulation of micro-objects is possible. In this paper, we develop a two-dimensional (2D), computer vision-based, force sensing device which consists of an elastic mechanism with known

force-deflection characteristics. From observing the deformation of a calibrated structure as it interacts with an object that it is manipulating, the actual manipulation force can be extracted.

2. Related work

The few commercially available micro-force sensors are only capable of measuring one dimensional forces and requires extensive (proprietary) hardware, software, as well as, in some cases, a high resolution scanning electron microscope to function [14–16]. Thus, the development of micro-force sensors has been an active research topic of late. An overview of force sensing for microassembly applications is given in [17] while a review of MEMS devices used for cellular force measurements can be found in [18]. An atomic force microscope (AFM) is commonly used to measure small forces, in the pN to nN range [19]. However, Sitti used an AFM for manipulation along with integrated force sensing at the mN level in [20]. Koch et al. [21] designed, fabricated, and tested a compliant surface-micromachined spring in order to calibrate the lateral force field of an electromagnet on a single magnetic microparticle. In [11], a micro-force sensing silicon cantilever beam that has two resistors deposited to its opposite sides is presented. When the beam is bent, the areas where the resistors are located are deformed and the piezoresistive effect of silicon resistors cause changes in resistance related to the strain in the beam from which force values can be extracted. While a large range of forces (nN to mN) can be measured, they are only done so in one-dimension and specialized electronics and signal conditioning is required for accurate results. Piezoresistors were also added to low temperature co-fired

* Corresponding author. Current address: Department of Mechanical Engineering, Stevens Institute of Technology, Hoboken, NJ, USA. Tel.: +1 2012165072; fax: +1 2012168315.

E-mail addresses: dcappell@stevens.edu (D.J. Cappelleri), piazza@seas.upenn.edu (G. Piazza), kumar@seas.upenn.edu (V. Kumar).

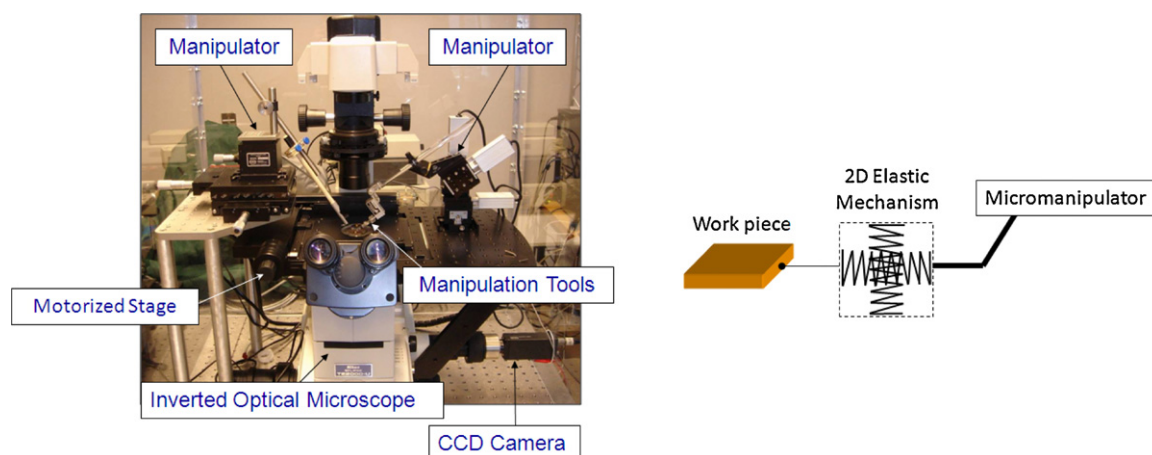


Fig. 1. Microrobotic test-bed (left); force sensor design schematic (right).

ceramic beams in [22] and demonstrated to sense mN level forces in one dimension.

In regards to vision and optical force sensing, a 5 mm diameter tri-axial force sensor was developed in [23] based on a flexible titanium structure of which the deformations are measured through reflective measurements with three optical fibres. It has a range of 2.5 N in axial direction and 1.7 N in radial direction, with resolutions of 0.01 N. The design for a micrograting-based force sensor integrated with a surface micromachined silicon-nitride probe for penetration and injection into drosophila embryos is presented in [24,25]. Optics are also used in [26,27] to sense contact forces. A minimally intrusive, vision-based, computational force sensor for elastically deformable objects is presented in [28]. Greminger et al. demonstrates a method to visually measure the force distribution applied to a linearly elastic object using the contour data in an image in [29]. Sasoglu et al. have used high-aspect ratio polydimethylsiloxane (PDMS) microbeams to sense one dimensional micro-scale forces specifically targeted for single cell studies [30]. Similar PDMS beam structures have been used by Liu et al. [31] to hold a cell in place during microrobotic mouse embryo injection while tracking the beam displacements, thus extracting force information.

Our design, which allows for two-dimensional sensing of micro-forces, can be easily integrated into standard robotic manipulation test-beds without cluttering the workspace or requiring any complicated drive electronics. It can also be used as a manipulation tool to execute a variety of tasks and is applicable to many different applications. The modeling, design, microfabrication, calibration and experimental validation of this force sensor for use in a robotic manipulation task of microassembly along with some preliminary results for next generation force sensor designs are presented.

3. Force sensor design

The μN force sensor design presented here is intended for use in the micro/meso-scale robotic manipulation test-bed that is pictured in Fig. 1(left). For manipulation at these scales, surface forces, such as stiction, friction, and electrostatic forces, dominate. Most parts are planar so access to the parts from the top is generally possible. Grasping the part with a suction gripper is possible, however it can only be used to approximately position the parts due to the difficulties in part release resulting from dominate surface forces. Therefore, we use manipulators (probes) with one or more point contacts to position parts. The approach for the force sensor design can be seen schematically Fig. 1(right). We want to design a two-dimensional elastic mechanism that can be directly mounted to

the micro-manipulator at one end, while the other end can be used to manipulate parts by pushing on them with one or more point contacts. The device needs to be designed with geometry that can be tracked in two dimensions in the images from the CCD camera, providing two-dimensional (in the XY-plane) μN level force sensing.

3.1. Force sensor specifications

The specific performance specifications for the force sensor are dictated by the constraints imposed by the vision system in the microrobotic test-bed and particular application. A probing section of the force sensor mechanism with tracking points along with a fixed, stationary point need to be in the microscope field of view (FOV) at all times so they can be observed by the CCD camera and displacement information extracted and converted to manipulation forces using the device's stiffness calibration data. The constraints imposed by the vision system are dependant on the choice of microscope objective. For example, when using the $4\times$ objective in our system the size of the FOV is $3.368\text{ mm} \times 2.626\text{ mm}$, with an image resolution of $5.26\text{ }\mu\text{m}/\text{pixel}$. However, with a $40\times$ objective, the FOV reduces to $344\text{ }\mu\text{m} \times 258\text{ }\mu\text{m}$, with a corresponding image resolution of $0.537\text{ }\mu\text{m}/\text{pixel}$. (Note: the accuracy of the vision-based force sensor is not necessarily equal to the image resolution. Rather, it corresponds to the robustness and accuracy of the feature tracking algorithm utilized.)

Two initial application areas are considered when designing these vision-based force sensors: meso/micro-scale assembly and biological cell manipulation. The design specifications for each of these are listed in Table 1. In the case of meso/micro-scale assembly, large deflections ($\geq 1\text{ pixel} = 5.26\text{ }\mu\text{m}$) are required to be able to optically track them with the camera. The larger objective and corresponding smaller FOV that is used with cell manipulations will require much smaller deflections to be observed. The maximum deflection values listed in the table are the maximum deflections allowed for the device to keep all necessary tracking points in the

Table 1
Design specifications per application area.

	Meso/micro-scale assembly	Cell manipulation
Expected force range	0–50 μN	0–10 μN
Characteristic length	1200 $\mu\text{m} \times 500\text{ }\mu\text{m}$	50–200 μm diameters
Objective	4 \times	40 \times
Desired resolution	0.25–0.75 $\mu\text{N}/\text{pixel}$	0.01–0.05 $\mu\text{N}/\text{pixel}$
XY stiffness range	0.05–0.15 N/m	0.025–0.100 N/m
Maximum deflection	200 μm	20 μm

FOV during a particular type of manipulation. Thus, the range for the designed sensor will be its XY stiffness \times this maximum deflection value. The desired resolution ranges for each of the applications are $0.25\text{--}0.75\text{ }\mu\text{N/pixel}$ and $0.01\text{--}0.05\text{ }\mu\text{N/pixel}$, respectively. This, along with the image resolution for the particular objective being used, determines the acceptable XY stiffness range for the force sensor. As stated previously, capacitive and piezoresistive strain gage MEMS sensors are capable of achieving similar resolutions but suffer from complicated manufacturing processes and require special drive electronics for operation. The advantages to our vision-based force sensor designs are that they can be easily integrated into standard microrobotic testbeds without the addition of this extra hardware, do not have a complicated fabrication process, and can sense forces in two-dimensions while also being used as a manipulation tool. In this paper, we are focusing on designing a device for the meso/micro-scale assembly application area. In order to maximize the sensitivity of the device, we want to minimize the $\mu\text{N/pixel}$ ratio. Thus, a device stiffness in each direction $\leq 0.05\text{ N/m}$ will result in sensor resolutions of at least 4 pixels/ μN .

3.2. Approach

The design principles and formulas used to design compression springs are leveraged here to derive some intuitive designs for the vision-based force sensor. We essentially want to design a low stiffness, two-dimensional spring. In order to design a low stiffness spring (structure) for a given design space and material, one needs to have many active coils and/or thin elastic members. These design principles have been utilized in the design of MEMS linear actuators, resonators, and accelerometers. Typically, these suspension designs have large displacements in the direction of actuation and high stiffness in the other two perpendicular directions and consist of spring-like, elastic flexure elements in various configurations along with a centrally located rigid shuttle mass [32]. The *simple suspension* and *crab-leg* design topologies were initially explored here. The shuttle mass geometry was modified to include a rigid probe section to be used for manipulation. The beam geometries were designed for low stiffness in both the lateral and transverse directions (switching from low stiffness in 1D to 2D) and nonlinear finite element analysis (FEA) performed. The material was taken to be silicon and no constraints on the design domain size enforced. The results produced beam dimensions that yielded stiffness in the desired range needed to sense μN level forces. However, the aspect ratios of the beam length:width and beam length:thickness were very large. Thus, the out-of-plane stiffness was too low causing the device to deform under its own weight. In order to avoid this problem, the design space needs to be fixed in size and a more sophisticated way to minimize the 2D stiffness of the structure in the given design space has to be developed.

3.3. Silicon designs \Rightarrow PDMS designs

The design methodology and procedure used to obtain the lowest stiffness design topology for a fixed design space is described in detail in [33] and is summarized in the following paragraphs. A Monte Carlo optimization of planar, spring-like structures, yielded a number of candidate designs. Macro-scale prototypes of these designs were manufactured out of acrylic using a laser cutter and the stiffness of each design in the X- and Y- direction were determined experimentally as k_x and k_y , respectively. Observations and conclusions were drawn from the experimental results which allowed for the designs to be refined by increasing the lengths of springs and changing their placements in order to provide even more improved (lower) stiffness values for a fixed design domain. Next, the dimensions of these macro-scale designs were scaled down to the micro-scale. Material properties for silicon were

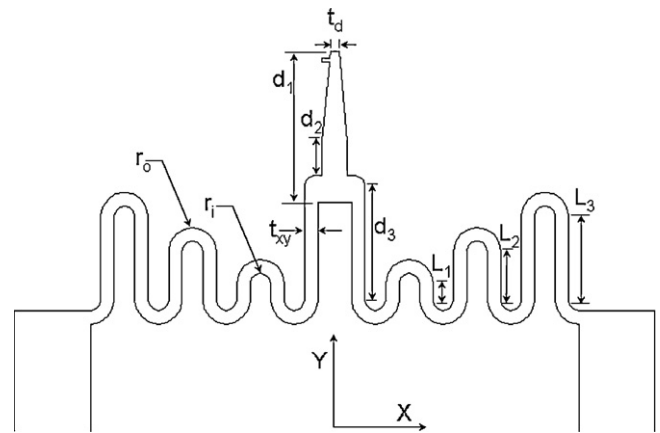


Fig. 2. PDMS prototype design parameters.

used to calculate corresponding stiffness values in the X- and Y-directions. While these designs did have much improved (lower) stiffness values than the original designs investigated and did not have the aspect ratio problems causing them to deform out-of-plane, the stiffness values were still not low enough to sense forces at the μN level. Therefore, we instead decided to use polydimethylsiloxane (PDMS) for the sensor design rather than silicon.

PDMS is a silicon-based organic polymer and is commonly used in microfluidic applications [34]. It is much softer than silicon ($E_{\text{PDMS}} = 360\text{ kPa}$ to $\sim 3\text{ MPa}$ [35,36] vs. $E_{\text{silicon}} = 160\text{ GPa}$ [37]) and using it for the designs instead of silicon allows for the minimum feature size of the devices to be increased for easier manufacturing while decreasing the overall footprint for the device to attain the same desired stiffness. Fig. 2 shows a schematic of a macro-scale prototype design that has a combination of both low X and Y stiffness values as well as high out-of-plane stiffness that was used as a starting point to optimize the design for the PDMS structures. A geometric description of the design is given by a set of design parameters, also shown in Fig. 2. The only parameter not defined in this figure is t_z , the out-of-plane beam thickness. This design is symmetric about the Y-axis and consists of a series of springs with varying number of turns (n) and link lengths (L_i 's).

A design parameter study was performed to come up with a set of feasible designs. The ranges for the design variables considered in the design parameter study were the following: n : 1–4; L_1 : 30–300 μm ; L_2 : 125–250 μm ; L_3 : 125–250 μm ; L_4 : 125–250 μm , d_1 : 250–450 μm ; d_2 : 50–100 μm ; and d_3 : 200–590 μm . For each design scenario considered, a linear finite element analysis was used to predict theoretical stiffness values in both the X- and Y-directions. From this analysis, fourteen designs were identified to meet the design requirement of 0.05 N/m maximum stiffness along each direction. The corresponding geometric descriptions for these designs are presented in Table 2 along with their stiffness values, while they are pictured schematically in Fig. 3.

4. Force sensor fabrication

Microfabricating these force sensor designs out of PDMS requires a slightly more complicated manufacturing process than if they were to be made just out of silicon. A mold first needs to be created that the PDMS material can be poured into, allowed to cure, and then the parts released or extracted from. The micro-fabrication process begins with spin-coating KMPR 1050 negative photoresist (MicroChem, www.microchem.com) onto a clean silicon wafer (Fig. 4(a)) followed by soft-baking on a hot plate for 30 min @ 105 $^{\circ}\text{C}$. A corresponding negative mask is then used in the photolithography step (Fig. 4(b)). The mask defines the geometry of

Table 2
Prototype geometric descriptions and stiffness values.

Design	n	L_1 (μm)	L_2 (μm)	L_3 (μm)	L_4 (μm)	d_1 (μm)	d_2 (μm)	d_3 (μm)	k_x (N/m)	k_y (N/m)
P1	4	250	250	250	250	450	100	340	0.0007	0.0010
P2	4	125	125	125	125	450	100	340	0.0033	0.0037
P3	4	125	125	125	125	450	100	200	0.0032	0.0036
P4	3	250	250	250	–	450	100	340	0.0023	0.0053
P5	3	125	125	125	–	450	100	200	0.0042	0.0078
P6	2	250	250	–	–	450	100	340	0.0033	0.0144
P7	1	500	–	–	–	450	100	590	0.0023	0.0266
P8	1	500	–	–	–	250	50	590	0.0036	0.0500
P9	2	250	250	–	–	250	50	340	0.0064	0.0144
P10	3	50	145	250	–	450	100	340	0.0025	0.0060
P11	2	125	250	–	–	450	100	340	0.0033	0.0149
P12	2	50	250	–	–	450	100	340	0.0034	0.0152
P13	2	35	250	–	–	450	100	340	0.0035	0.0152
P14	2	30	250	–	–	450	100	340	0.0035	0.0153

Constants: $r_i = 30 \mu\text{m}$, $r_o = r_i + t_{xy}$, $t_d = 25 \mu\text{m}$, $t_{xy} = 40 \mu\text{m}$, $t_z = 50 \mu\text{m}$.
Material properties: $E_{\text{PDMS}} = 615 \text{ kPa}$, Poisson's ratio $\nu = 0.48$.

the entire device. The wafer and mask are then exposed to 365 nm, 5 mW/cm² intensity, UV light with soft-contact for 3 min and then a post-exposure bake (PEB) @ 105 °C for 4 min 15 s is administered to the wafer. In order to help with the release of the cured PDMS device, the patterned wafer is then exposed to CF₄ plasma for 1 min using a RIE machine [38](Fig. 4(d)). PDMS (Dow Corning Sylgard 184 elastomer base and curing agent, www.dowcorning.com) is then mixed with a base:cure ratio of 12.5:1 (by weight) and spin-coated onto the wafer, Fig. 4(e), and cured. The curing procedure presented in [34] was modified to include clamping of the patterned wafer with PDMS between two aluminum plates with four C-clamps, one at each corner, and placing it in an oven for 3 h @ 100 °C. It is then allowed to cool overnight back down to room temperature before clamp removal. The planarization of the PDMS, shown in Fig. 4(f), can be done one of two ways with either laser etching or wet etching. Discussion of these two techniques will be presented shortly. After planing the PDMS, the photoresist (KMPR) is dissolved by placing the wafer in Remover-PG (MicroChem) solution for about 30 min while in a sonicator @ 60 °C, Fig. 4(g). The wafer is then placed in an acetone bath for approximately 20 h to swell the PDMS parts and make their extraction easier. The parts are extracted by peeling them off the wafer with tweezers, Fig. 4(h). Beryllium copper bases for the devices were manufactured with a photochemical machining process, courtesy of Fotofab (www.fotofab.com). They have nominal dimensions of 2.3 mm × 2.3 mm × 152.4 μm and are

used to provide rigidity to the base (handle) portion of the device. These base parts are epoxied to the base section of the PDMS force sensor, which is then epoxied to the end of a tungsten probe, completing the fabrication process (Fig. 4(i)).

Planing of the PDMS was done successfully with both laser etching and wet etching techniques. The laser etching was done with the ULS X-660 laser cutter with a 50 W CO₂ laser. Vector cuts of 75 μm spaced horizontal lines at speed and power settings of 30% and 2%, respectively, were typically used. When the KMPR layer on the wafer is reached with the laser it turns a yellowish color. Multiple passes with the laser etching at the specified settings were carried out as necessary until this phenomenon was observed. A problem with this technique is that the PDMS is not etched uniformly across the entire wafer and some of it can remain attached to the silicon substrate after the KMPR photoresist has been removed. This residue can interfere with the delicate spring and tip regions of the parts. This can be seen in some of the images shown in Fig. 5. Also, the laser etching leaves an uneven surface on top of the parts which will make it difficult to model accurately and determine force–displacement relationships. Never-the-less, these laser etched parts were able to be extracted from the silicon substrate and assembled to the beryllium copper parts. Examples of two of the PDMS–beryllium copper subassembly can be found in Fig. 6 along with schematics of some the nominal dimensions for the fabricated PDMS parts.

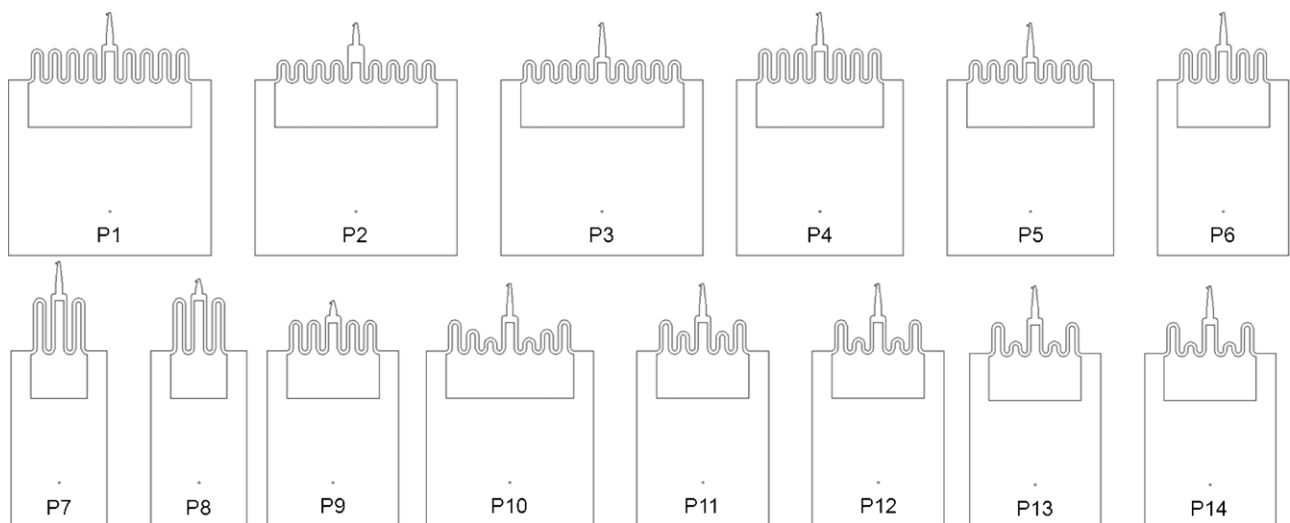


Fig. 3. PDMS prototype designs.

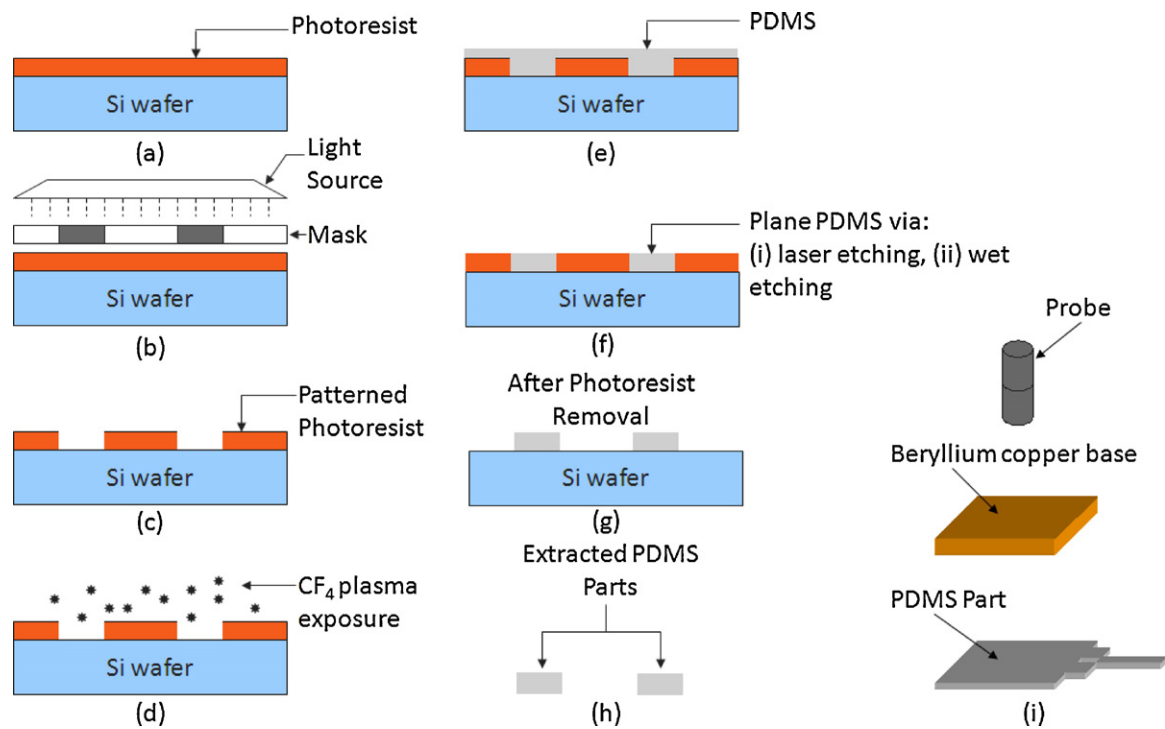


Fig. 4. Microfabrication process.

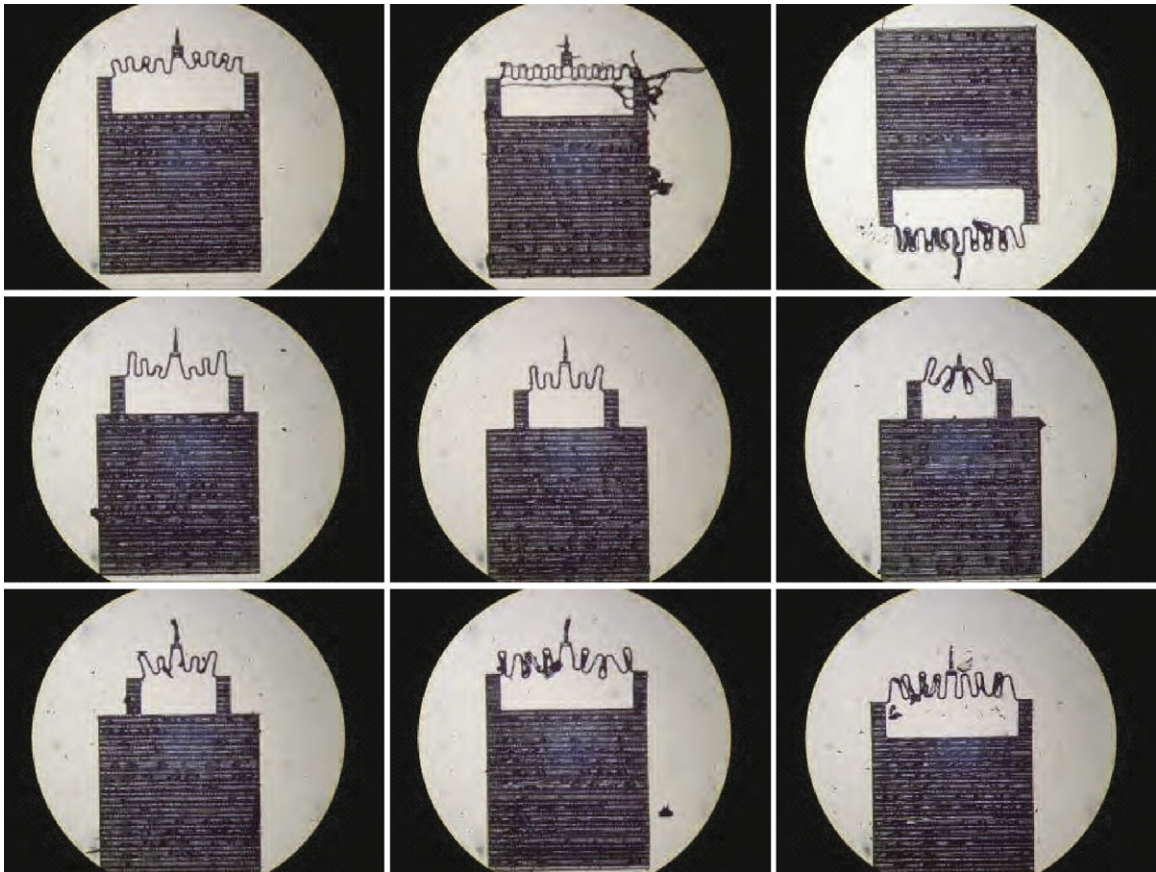


Fig. 5. Laser etched parts on substrate after KMPR removal.

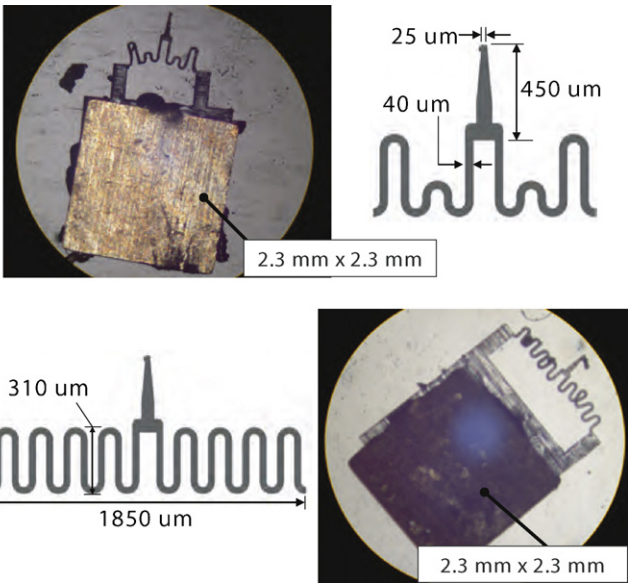


Fig. 6. Assembled laser etched parts.

In an effort to get cleaner, more defined features for the PDMS parts, planing of the PDMS in step (f) was explored with wet etching. Examples of wet etching of PDMS can be found in [39–41] and a similar recipe used there has been used here. A solution of tetrabutylammonium fluoride (TBAF) in N-methylpyrrolidone (NMP) (3:1; v/v; NMP/75%TBAF in water) is used as the PDMS etchant. The wafer is submerged in the solution for 10 min and then placed

in a DI water bath for 3 min. The rest of the process steps remain unchanged. Fig. 7 shows the wet etched parts on the silicon substrate after the removal of KMPR. The parts do appear much cleaner and have more defined features.

Subassemblies, consisting of the beryllium copper bases and extracted PDMS parts, are shown in Fig. 8(left). Note: the thicker the part is, the easier it is to remove it from the substrate. Therefore, PDMS parts thicker than the original design value (50 μm) were fabricated. This was also done to compensate for the unknown wet etch rates a priori. The thicker the PDMS parts, the stiffer the force sensor. Since the finite element analysis on the original design geometries predicted stiffnesses much lower than the required stiffness values, increasing the thickness of the devices will still produce force sensors that meet the stiffness requirement. One of the subassemblies from Fig. 8 is shown in more detail on the right side of the figure. Table 3 lists all of the measured design parameters for this prototype. These dimensions most closely resemble those of design P12 from Table 2. A tungsten probe was fastened to this prototype subassembly with epoxy, completing the fabrication process, as seen in the top right of Fig. 8.

5. Force sensor calibration

5.1. Material testing

The stiffness of the prototype is determined by the part geometry and the PDMS material properties. The Poisson's ratio for PDMS is known to be ≈0.5 [35]. The elastic modulus has a known range of 360 kPa–3 MPa, which varies based on curing agent:base solution ratio as well as other processing parameters and therefore needs

Table 3
Geometric description for fabricated PDMS prototype.

Design	<i>n</i>	<i>L</i> ₁ (μm)	<i>L</i> ₂ (μm)	<i>L</i> ₃ (μm)	<i>L</i> ₄ (μm)	<i>d</i> ₁ (μm)	<i>d</i> ₂ (μm)	<i>d</i> ₃ (μm)
Proto P12	2	60	384	–	–	671	147	502

Constants: *r*_i = 45 μm, *r*_o = *r*_i + *t*_{xy}, *t*_d = 28 μm, *t*_{xy} = 56 μm, *t*_z = 176 μm.

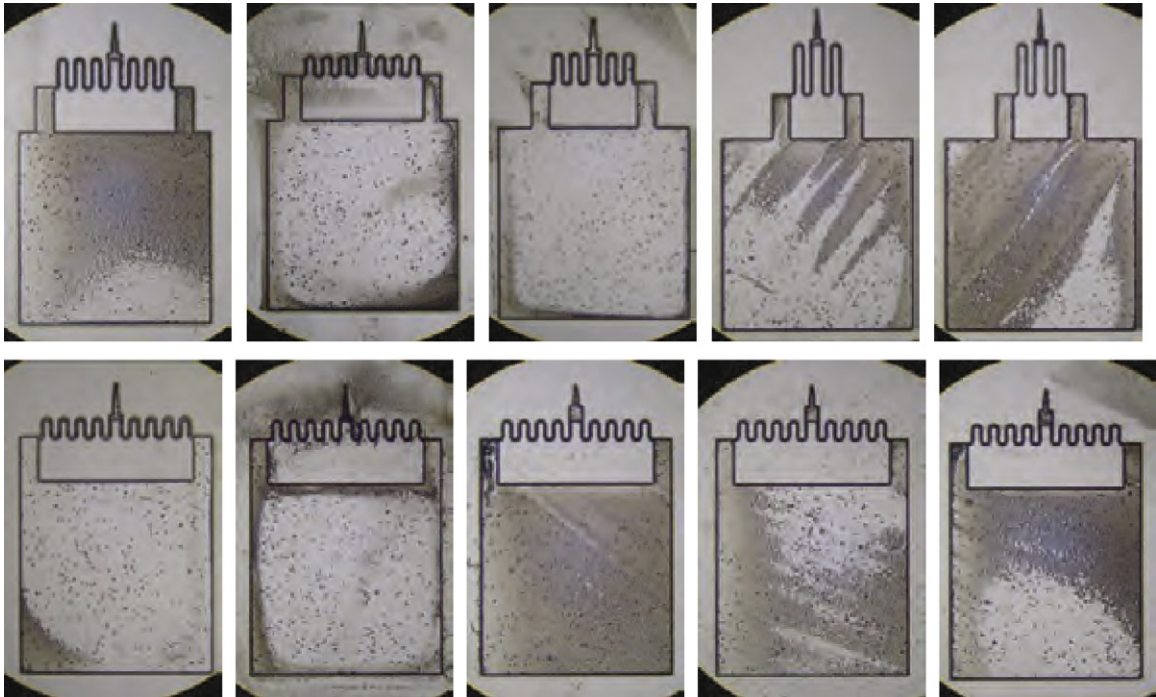


Fig. 7. Wet etched parts on substrate after KMPR removal.

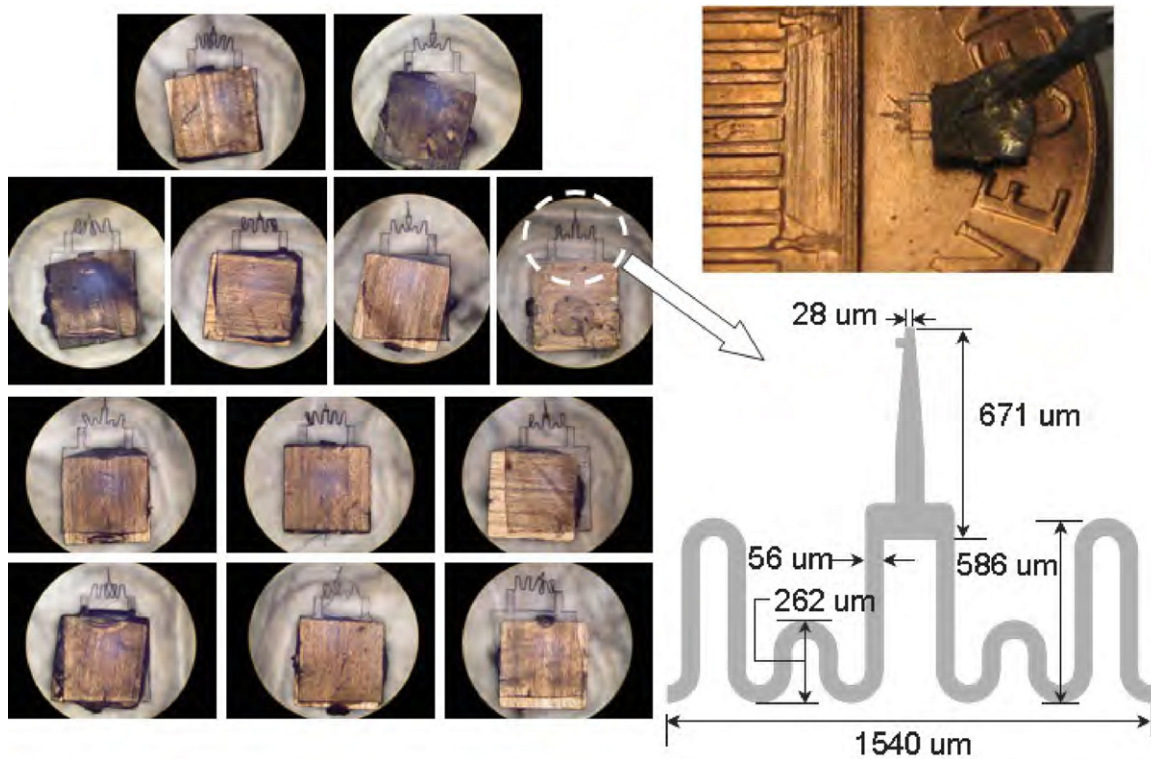


Fig. 8. Prototype subassemblies and selected prototype schematic.

to be tested for on a per wafer basis. PDMS samples from the same wafer as *Proto P18* without spring and tip sections (i.e. only the handle section) were used for material property tests. The modulus of elasticity of these samples were tested for with compression tests on an Instron 4206 machine and 10 N load cell. The samples started with a slight pre-load and then were loaded up to 45 g (~ 440 mN). Three samples were tested three times each and their corresponding stress–strain curves plotted in which the slopes yield the elastic modulus values for the particular sample. The average elastic modulus for the samples was taken as the elastic modulus for the device, 333.4 kPa. This value is at the low end of the range of published values for E_{PDMS} .

5.2. AFM nanoindentation tests

Atomic force microscope (AFM) nanoindentation tests were also performed on the prototype to determine its horizontal and vertical stiffness values. A calibrated AFM cantilever was used to apply a known force to the device that is mounted below it. The cantilever was first lowered to contact a rigid sample to determine the deflection sensitivity of the cantilever. From knowing this and the cantilever stiffness (K_{AFM}), this displacement data can be converted to force data to create a force–distance curve.

For these nanoindentation tests, the system can be modeled as three springs in series, as shown in Fig. 9(a), and the value for the

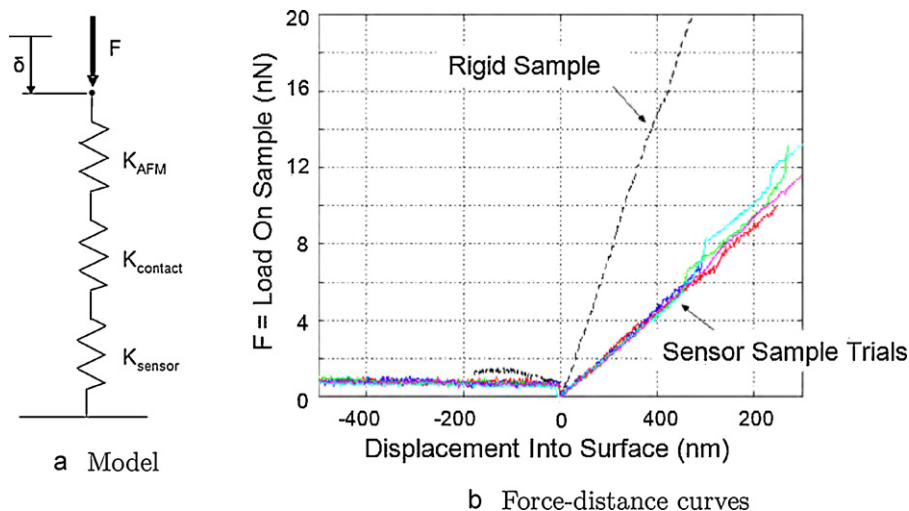


Fig. 9. AFM calibration tests.

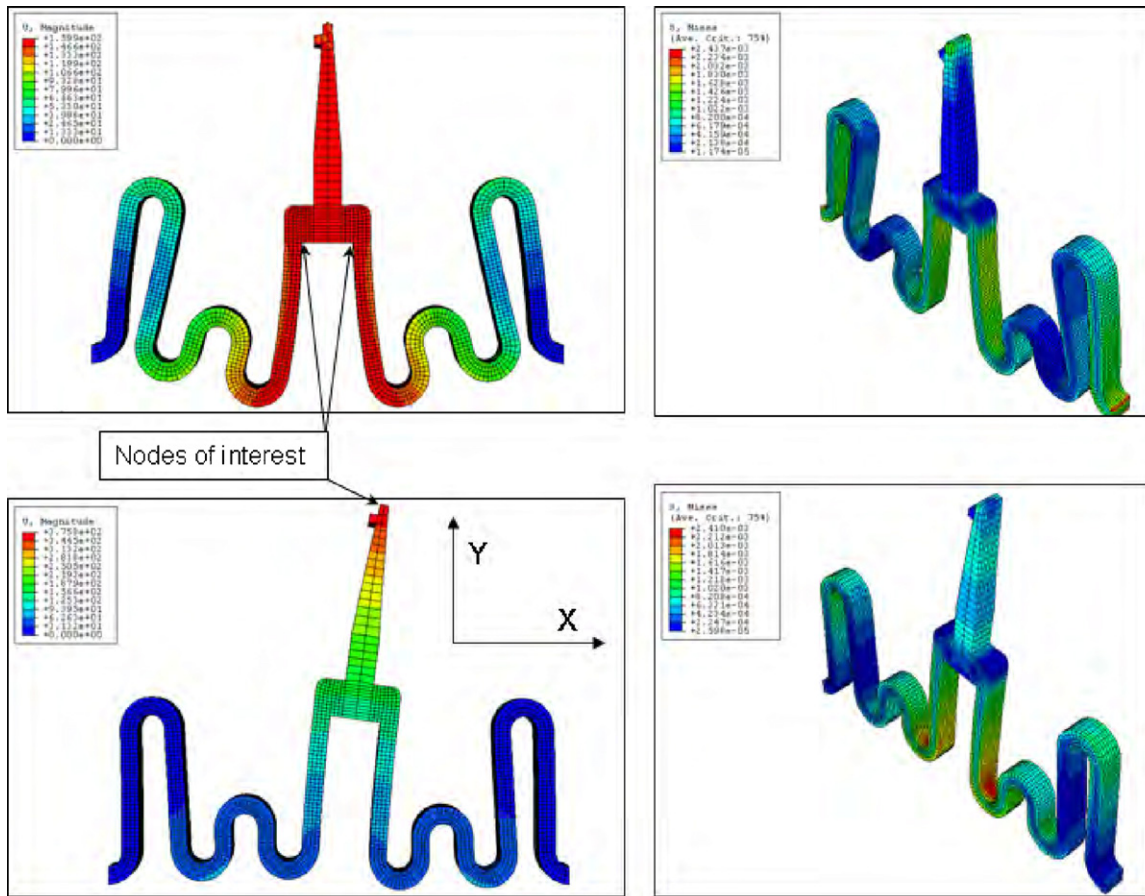


Fig. 10. Prototype finite element analysis for a single loading scenario.

stiffness of the device directly calculated from the AFM test data and the equation:

$$\delta = \left(\frac{1}{K_{AFM}} + \frac{1}{K_{contact}} + \frac{1}{K_{sensor}} \right) F \quad (1)$$

where δ is the photodiode displacement, F is the load applied to the sample, K_{sensor} is the sensor stiffness, K_x or K_y , depending on the mounting orientation, and $K_{contact}$ = contact stiffness for PDMS. K_{AFM} is known from AFM calibration tests [42] and δ and F are results from the indentation test data. The contact stiffness was first solved for by conducting an indentation test on a thick PDMS substrate section of the device so that $K_{sensor} = 0$ and $K_{contact}$ can be directly solved for.

Separate tests were performed to determine K_{sensor} , corresponding to K_x and K_y . At least 5 trials for each test were performed and force–distance curves were plotted for the compliant samples on the same axes as the data from a rigid sample to extract the corresponding δ and F values. The force–distance curves from the horizontal stiffness tests are shown in Fig. 9(b). Average values across all the trials were used to determine the experimental stiffness values. These tests produced stiffness values of $K_x = 0.0365$ N/m and $K_y = 0.0660$ N/m. FEA of the prototype using E_{PDMS} from the compression tests and the measured part geometry (Table 3) yielded stiffness values with roughly the same K_y/K_x ratio as the AFM calibration tests but with much lower stiffness values: $K_x = 0.00282$ N/m and $K_y = 0.00675$ N/m. This discrepancy in stiffness values between the finite element model and the AFM tests can be attributed to misalignment between the AFM tip and sensor angles and the facts that (1) the PDMS has a non-linear stiffness that depends on the loading force range and (2) nanoindentation tests

are known to produce higher material stiffnesses values than traditional compression test results for PDMS [43]. The AFM indentation tests done here correspond to a very low loading force range (nN). Differently, the loads from the compression tests are in the μ N to mN range. Therefore, it is reasonable that stiffness values from the nanoindentation tests are much higher. Since the device will not be operating in such a low force regime for this application, the E_{PDMS} from the compression tests, corresponding to the lower device stiffness values, were used in finite element models to determine the force–displacement relationship for the device while subjected to μ N loads at various angles in the XY-plane.

5.3. Calibration curves

We conducted finite element analysis (FEA) with various loads at varying angles applied to the tip of the device, as seen in Fig. 10. Only the spring and tip section of the part is analyzed since the base section is a rigid structure. The anchor point for the springs have fixed boundary conditions. The part is meshed with 8-node, linear, brick elements and analysis runs are executed with various loads at varying angles applied to the tip of the device. Loads with magnitudes of 0.1, 0.25, 0.50, 0.75, 1, 2, 3, 4, 5, and 10 μ N are each applied at angles of 0°, 15°, 30°, 45°, 60°, 75°, and 90°. A force angle of 0° and 90° corresponds to loads only in the Y-direction and X-direction, respectively, according to the coordinate system found in Fig. 10. Displacement values corresponding to the change in distance between the tracking points $N_t = (X_t, Y_t)$, $N_b = (X_b, Y_b)$, and $N_{tip} = (X_{tip}, Y_{tip})$ relative to the stationary (fixed) point, $N_f = (X_f, Y_f)$, in Fig. 11(a) were recorded for each run. The displacement data for all three tracking nodes for the various runs was compiled in

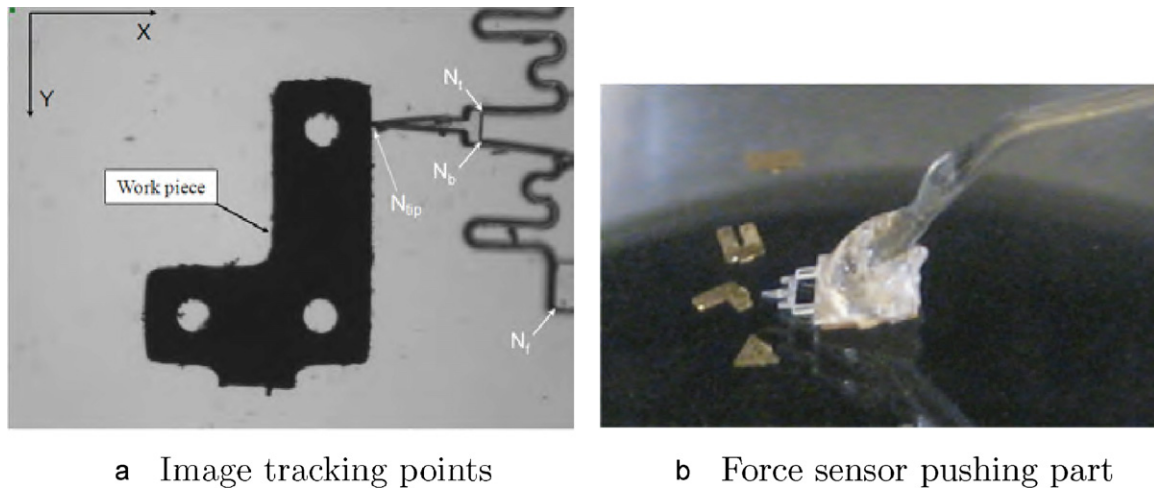


Fig. 11. Micromanipulation experiments.

μm and converted to corresponding image pixels using the image resolution for the 4X microscope objective (i.e. $5.26 \mu\text{m}/\text{pixel}$). This FEA data was used to compute a quadratic calibration curve for the force sensor in the form of:

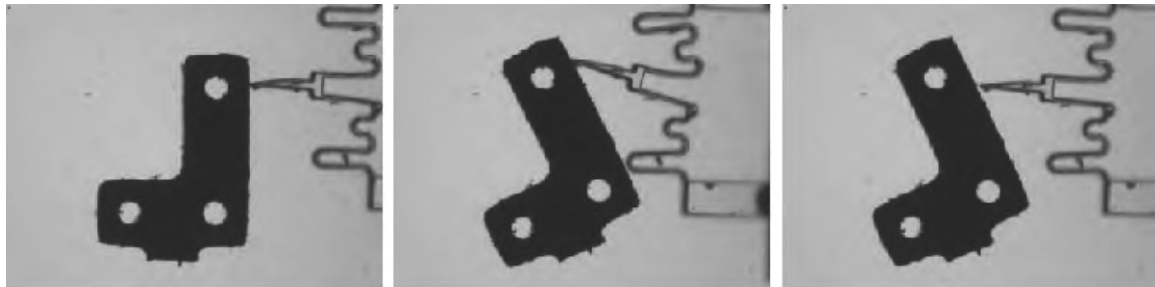
$$F = \beta_0 + \beta_1(\Delta X) + \beta_2(\Delta Y) + \beta_{12}(\Delta X)(\Delta Y) + \beta_{11}(\Delta X)^2 + \beta_{22}(\Delta Y)^2 \quad (2)$$

where F is either the X - or Y -direction force, F_x or F_y , and ΔX and ΔY correspond to displacements of a particular node of interest. The FEA data was first transformed to the image coordinate system to correspond to displacement components for the nodes of interest: ΔX_t , ΔY_t , ΔX_b , ΔY_b , ΔX_{tip} , and ΔY_{tip} (in pixels) and forces F_x and F_y (μN) according to the axes shown in Fig. 11(a). Matlab[®] was used to perform regression analysis and solve for the unknown β terms,

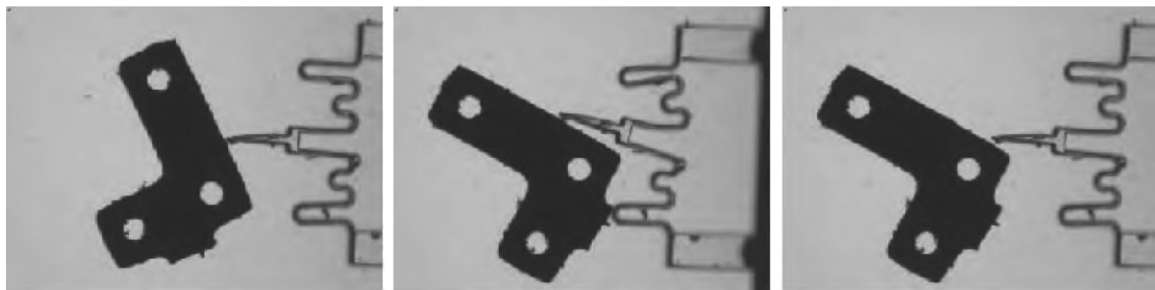
which vary with the different choices for the input variables, with a 99% confidence interval.

6. Experimental manipulation results for microassembly

The fully assembled prototype was mounted to the 4-axis computer controlled manipulator in the experimental test-bed shown in Fig. 1(left) to test the viability of the prototype for force-guided micro- and meso-scale assembly tasks. Meso-scale beryllium copper parts were placed on a glass microscope slide and experimental test pushes with the force sensor on the parts executed. Fig. 11(b) shows the force sensor about to push one of the test parts while Fig. 12 shows screen shots from two test pushes executed back-to-back in the system test-bed. In order to extract force information from the captured images, the displacements of the device in each image frame needed to be tracked accordingly. Four tracking points



a Test push 1: Initial, intermediate, and final configurations



b Test push 2: Initial, intermediate, and final configurations

Fig. 12. Snapshots from experimental test pushes.

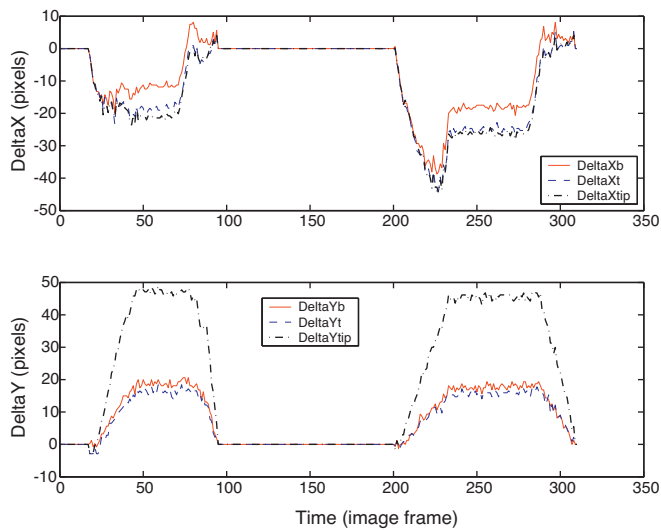


Fig. 13. Displacement data from test pushes.

on the prototype force sensor were designated for tracking and are shown in Fig. 11(a). Points N_t , N_b , and N_{tip} move when force is applied at the tip. Point $N_f = (X_f, Y_f)$ is a fixed position on the device that does not change when the tip encounters a force. By tracking the positions of any of the moving points along with the fixed point in each image frame, displacement data for the device is extracted. Image processing was performed to extract this information and it can be found in Fig. 13 for these two test pushes. Note the image coordinate system (shown in Fig. 11(a)) is being used to report the displacements. Since the points N_b , N_t , and N_{tip} all reside on the rigid, probe section of the device, their displacements coincide with each other. The displacement values for N_t and N_b are essentially identical due to the device symmetry. The values for the tip displacements are larger because they are magnified by the moment arm distances from the locations of the other tracking points on the same rigid body. Three models, corresponding to each tracking point's displacement data, were created to calculate the X- and Y-direction forces corresponding to the two test pushes. The orientation of the part was also tracked and used to convert the X- and Y-component forces to normal (n -) and tangential (t -) directional forces. The results from all the models are consistent. Plots of the force trajectories for the test pushes, using each of the models, are shown in Fig. 14. The tracking point N_{tip} was obstructed by the part being manipulated in some instances. This resulted in slight differences from the force values extracted from the corresponding model (M3) when compared to the other models using tracking points N_t or N_b (M1 and M2, respectively), that were not obstructed during the pushes. Therefore, we restrict our results to

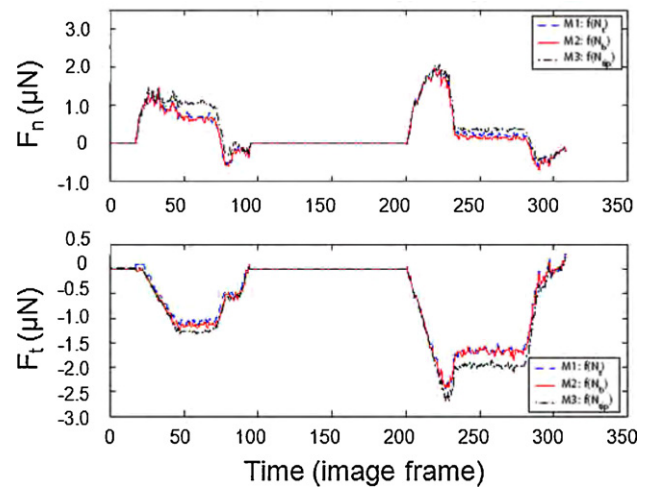


Fig. 14. Experimental pushing forces.

Table 4

Maximum and minimum pushing forces.

Model	$F_{n_{max}}$ (μN)	$F_{n_{min}}$ (μN)	$F_{t_{max}}$ (μN)	$F_{t_{min}}$ (μN)
Push 1				
M1: $f(\Delta X_t, \Delta Y_t)$	1.4735	-0.5558	0.1111	-1.1382
M2: $f(\Delta X_b, \Delta Y_b)$	1.4553	-0.5907	0.0931	-1.2516
Push 2				
M1: $f(\Delta X_t, \Delta Y_t)$	1.9515	-0.6782	0.2423	-2.4473
M2: $f(\Delta X_b, \Delta Y_b)$	1.9708	-0.6961	0.1345	-2.4084

the values obtained from these tracking points and corresponding models, M1 and M2. The maximum n -direction force required to move the part in the first push was approximately $1.5 \mu\text{N}$, while it was $2.0 \mu\text{N}$ for the second push, as seen in Table 4. There are also high tangential forces required to overcome the surface frictional forces between the metal part and glass substrate, $1.2 \mu\text{N}$ and $2.4 \mu\text{N}$, respectively. These extracted force values are in the expected force range for pushing the part from rest. The required pushing force should be greater than or equal to the normal force (N) \times the coefficient of friction ($\mu_{friction}$). This value has been calculated to be $3.19 \mu\text{N}$ using the equations in Equation Set 3 and the parameters for $\mu_{friction}$ and the density of beryllium copper found in [44] and [45], respectively. The area of the part was determined from measurements with the optical microscope. Thus, this value compares quite well to the pushing forces determined for push 2 from the model predictions and therefore they appear valid.

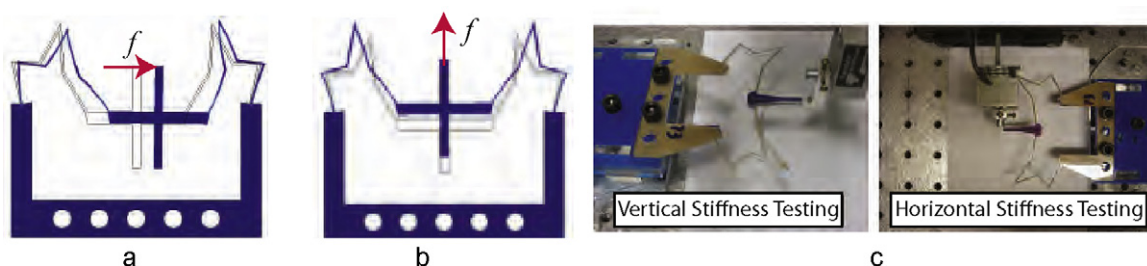


Fig. 15. Preliminary future work on designing decoupled force sensor designs wherein linear force yields parallel translation is shown in (a) and (b) [47]. Scaled-up prototypes fabricated from acrylic tested experimentally show promising results (c).

$$\begin{aligned}
 F_{\text{push}} &\geq \mu_{\text{friction}} N = 3.19 \mu\text{N} \\
 \mu_{\text{friction}} &= 0.5 \text{ (for glass/metal interface)} \\
 N &= \text{mass} \times \text{gravity} = 6.3824 \mu\text{N} \\
 \text{gravity} &= 9.81 \text{ m/s}^2 \\
 \text{mass} &= \text{volume} \times \text{density} = 6.5060 \times 10^{-7} \text{ kg} \\
 \text{density}_{\text{berylliumcopper}} &= 8100 \text{ kg/m}^3 \\
 \text{volume} &= \text{area} \times \text{thickness} = 8.0321 \times 10^7 \mu\text{m}^3 \\
 \text{thickness} &= 76.2 \mu\text{m} \\
 \text{area} &= 1.0541 \times 10^6 \mu\text{m}^2
 \end{aligned} \tag{3}$$

The difference in the forces between the two pushes is valid since in push 2, the pushing location was more centrally located, closer to the center of mass of the part, causing more of a translational motion of the part, thus requiring larger forces.

The performance of the force sensor can now be evaluated against the design requirements. These design requirements were stated earlier as trying to minimize the $\mu\text{N}/\text{pixel}$ ratio, with $K_x, K_y \leq 0.05 \text{ N/m}$, corresponding to a resolution of at least $0.25 \mu\text{N}/\text{pixel}$ (4 pixels/ μN). FEA of the prototype, with the measured dimensions and E_{PDMS} from the compression tests, yielded stiffness values of $K_y = 0.0136 \text{ N/m}$ and $K_x = 0.00738 \text{ N/m}$. This is calculated as the ratio of the applied force and the displacement of the sensor tracking point (N_t or N_b). These stiffness values correspond to 14 and 26 pixels/ μN resolutions along the Y- and X- axis, respectively. Thus, the designed and fabricated prototype does indeed meet the design requirements.

7. Conclusions and future work

A proof-of-concept prototype of a 2D, compliant mechanism, vision-based force sensor has been described in this paper. The sensor does not require any additional instrumentation to be added to a standard microrobotic manipulation test-bed and can be used to sense both displacements and forces as well as used as a manipulation tool. We performed experimental tests and FE modeling in order to benchmark and calibrate a microfabricated PDMS prototype. Absolute calibration of the device is hard because of the difficulties in characterizing soft, viscoelastic materials like PDMS.

Extensive experimentation needs to be conducted before this device can be turned into a commercial product. The repeatability for the sensor needs to be quantified as well as some measure of the life cycle for a particular sensor identified from testing many prototypes. Our future work is in both of these areas and in designing structures with decoupled displacements at the tracking points and equal stiffness along each axis for easier force extraction. For the decoupled designs, we will use the building block approach for conceptual synthesis of the compliant mechanism design for the force sensor [46]. The compliance and stiffness ellipses for the mechanism can be constrained to be circular while the magnitudes for the corresponding stiffness and compliance coupling vectors can be fixed to zero in order to satisfy the design requirements of decoupled motions along with equal stiffness along the X and Y axes of the mechanism [47]. These designs can be easily scaled up or down and the experimental testing of macro-scale prototypes of some of these new designs, shown in Fig. 15, are promising. We hope that the observations and analysis learned from this study will guide us in our future work of realizing micro-scale, decoupled, two-dimensional, vision-based μN force sensors to be used for micro-scale robotic manipulation and assembly tasks. Nevertheless, the proof-of-concept micro-scale prototypes presented here are the first step in producing a viable, low cost, commercial prod-

uct that can be easily integrated into standard micromanipulation systems to sense 2D μN level forces in microrobotic applications.

Acknowledgments

We gratefully acknowledge the support of NSF Grant IIS-0413138, Dept. of Education GAANN Grant P200A060275, and the Keck Foundation; Joe Grogan for his help in the microfabrication of the force sensor prototypes at the Wolf Nanofabrication Lab, University of Pennsylvania, and Prof. Robert Carpick and Graham Wabiszewski for discussions regarding the AFM calibration tests and help with and use of the Quesant AFM in the Carpick Research Group lab.

Appendix A. Supplementary data

Supplementary data associated with this article can be found, in the online version, at doi:10.1016/j.sna.2011.06.014.

References

- [1] S. Fatikow, U. Rembold, *Microsystem Technology and Microrobotics*, Springer, New York, 1997.
- [2] J. Thompson, R. Fearing, Automating microassembly with ortho-tweezers and force sensing, in: IEEE/RSJ International Conference on Intelligent Robots and Systems (IROS), Maui, HI, USA, 2001.
- [3] A. Hoover, R. Fearing, Rapidly prototyped orthotweezers for automated microassembly, in: IEEE International Conference on Robotics and Automation (ICRA), Rome, Italy, 2007.
- [4] Y. Yamamoto, R. Konishi, Y. Negishi, T. Kawakami, Prototyping ubiquitous micro-manipulation system, in: Proceedings of the IEEE International Conference on Advanced Intelligent Mechatronics (AIM), 2003.
- [5] R. Perez, N. Chaillet, et al., Fabrication, modeling and integration of a silicon technology force sensor in a piezoelectric micro-manipulator, *Sensors and Actuators A: Physical* 128 (2006) 367–375.
- [6] E. Enikov, B. Nelson, Three-dimensional microfabrication for a multi-degree-of-freedom capacitive force sensor using fibre-chip coupling, *Journal of Micromechanics and Microengineering* 10 (2000) 492–497.
- [7] Y. Sun, B. Nelson, D. Potasek, E. Enikov, A bulk microfabricated multi-axis capacitive cellular force sensor using transverse comb drives, *Journal of Micromechanics and Microengineering* 12 (2002) 832–840.
- [8] Y. Sun, D. Potasek, D. Piyongkarn, A. Sezen, R. Rajamani, B. Nelson, Actively servoed multi-axis microforce sensors, in: Proceedings of the 2003 IEEE International Conference on Robotics and Automation, Taipei, Taiwan, 2003.
- [9] F. Beyeler, A. Neild, S. Overt, D. Bell, Y. Sun, J. Dual, B. Nelson, Monolithically fabricated micro-gripper with integrated force sensor for manipulating micro-objects and biological cells aligned in an ultrasonic field, *IEEE/ASME Journal of Microelectromechanical Systems (JMEMS)* 16 (1) (2007) 7–15.
- [10] S. Muntwyler, F. Beyeler, B.J. Nelson, Three-axis micro-force sensor with tunable force range and sub-micronewton measurement uncertainty, in: Proceedings of the IEEE International Conference on Robotics and Automation (ICRA), 2010.
- [11] X. Li, D. Su, Z. Zhang, A novel technique of microforce sensing and loading, *Sensors and Actuators A: Physical* 153 (2009) 13–23.
- [12] P. Cheng, D. Cappelleri, B. Gavrea, V. Kumar, Planning and control of meso-scale manipulation tasks with uncertainties, in: Proceedings of Robotics: Science and Systems, Atlanta, GA, USA, 2007.
- [13] D. Cappelleri, J. Fink, B. Mukundakrishnan, V. Kumar, J. Trinkle, Designing open-loop plans for planar micro-manipulation, *IEEE International Conference on Robotics and Automation*, Orlando, FL.
- [14] SensorOne, AE801, http://sensorone.com/ae801_home.asp.
- [15] Zyver Instruments Force Characterization Package, www.zyver.com.
- [16] FemtoTools FT-S probes, www.femtotools.com.
- [17] B. Nelson, Y. Zhou, B. Vikramaditya, Sensor-based microassembly of hybrid MEMS devices, *IEEE Control Systems Magazine* 18 (6) (1998) 35–45.
- [18] Y. Sun, B. Nelson, MEMS for cellular force measurements and molecular detection, *International Journal of Information Acquisition* 1 (1) (2004) 23–32.
- [19] H.-J. Butt, B. Cappella, M. Kappl, Force measurements with the atomic force microscope: technique, interpretation and applications, *Surface Science Reports* 59 (2005) 1–152.
- [20] M. Sitti, Teleoperated and automatic nanomanipulation systems using atomic force microscope probes, in: 42nd IEEE Conference on Decision and Control, Maui, HI, USA, 2003.
- [21] S. Koch, G. Thayer, A. Corwin, M. de Boer, Micromachined piconewton force sensor for biophysics investigations, *Applied Physics Letters* 89, 173901.

- [22] H. Birol, T. Maeder, et al., Fabrication of a millinewton force sensor using low temperature co-fired ceramic (ltcc) technology, *Sensors and Actuators A: Physical* 134 (2007) 334–338.
- [23] J. Peirs, J. Clijnen, et al., A micro optical force sensor for force feedback during minimally invasive robotic surgery, *Sensors and Actuators A: Physical* 115 (2004) 447–455.
- [24] X. Zhang, C.-C. Chen, R. Bernstein, S. Zappe, M. Scott, O. Solgaard, Microoptical characterization and modeling of positioning forces on drosophila embryos self-assembled in two-dimensional arrays, *Journal of Microelectromechanical Systems* 14 (5) (2005) 1187–1197.
- [25] X. Zhang, S. Zappe, R. Bernstein, O. Sahin, C.-C. Chena, M. Fish, M. Scott, O. Solgaard, Micromachined silicon force sensor based on diffractive optical encoders for characterization of microinjection, *Sensors and Actuators A* 114 (2004) 197–203.
- [26] Y. Zhou, B. Nelson, The effect of material properties and gripping force on micro-grasping, in: *Proceedings of the IEEE International Conference on Robotics & Automation (ICRA)*, San Francisco, CA, 2000.
- [27] K.-H. Jeong, C. Keller, L. Lee, Direct force measurements of biomolecular interactions by nanomechanical force gauge, *Applied Physics Letters* 86, 19.
- [28] X. Wang, G. Ananthasuresh, J. Ostrowski, Vision-based sensing of forces in elastic objects, *Sensors and Actuators A* 94 (2001) 142–156.
- [29] M. Greminger, B. Nelson, Vision-based force measurement, *IEEE Transactions on Pattern Analysis and Machine Intelligence* 26 (3) (2004) 290–298.
- [30] F. Sasoglu, A. Bohl, B. Layton, Design and microfabrication of a high-aspect-ratio pdms microbeam array for parallel nanonewton force measurement and protein printing, *Journal of Micromechanics and Microengineering* 17 (2007) 623–632.
- [31] X. Liu, K. Kim, Y. Zhang, Y. Sun, Nanonewton force sensing and control in micro-robotic cell manipulation, in: *Proceedings of Robotics: Science and Systems IV*, Zurich, Switzerland, 2008.
- [32] L. Saggere, S. Kota, S. Cray, A new design for suspension of linear microactuators, *Proceedings of the International Mechanical Engineering Congress and Exposition: Dynamic Systems and Control*, Chicago, IL, ASME DSC 55 (2) (1994) 671–675.
- [33] D. Cappelleri, Flexible automation of micro and meso-scale manipulation tasks with applications to manufacturing & biotechnology, Ph.D. Dissertation, University of Pennsylvania, Philadelphia, PA, 2008 August.
- [34] B. Jo, L. Lerberghe, K. Motsegood, D. Beebe, Three-dimensional micro-channel fabrication in polydimethylsiloxane (PDMS) elastomer, *Journal of Microelectromechanical Systems* 9 (1) (2000) 76–81.
- [35] D. Armani, C. Liu, N. Aluru, Re-configurable fluid circuits by PDMS elastomer micromachining, in: *Twelfth IEEE International Conference on Micro Electro Mechanical Systems (MEMS)*, Orlando, FL, 1999.
- [36] F. Carrillo, S. Gupta, M. Balooch, S. Marshall, G. Marshall, L. Pruitt, C. Puttlitz, Nanoindentation of polydimethylsiloxane elastomers: effect of crosslinking, work of adhesion, and fluid environment on elastic modulus, *Journal of Materials Research* 20 (10) (2005) 2820–2830.
- [37] S. Senturia, *Microsystem Design*, Kluwer Academic Publishers, Boston, MA, 2003.
- [38] J. Kim, J. Park, S. Yang, J. Baek, B. Kim, S. Lee, E.-S. Yoon, K. Chunb, S. Park, Establishment of a fabrication method for a long-term actuated hybrid cell robot, *Lab on a Chip* 7 (2007) 1504–1508.
- [39] J. Garra, T. Long, J. Currie, T. Schneider, R. White, M. Paranjape, Dry etching of polydimethylsiloxane for microfluidic systems, *Journal of Vacuum Science and Technology A* 20 (3) (2002) 975–982.
- [40] B. Xu, F. Arias, G. Whitesides, Making honeycomb microcomposites by soft lithography, *Advanced Matter* 11 (6) (1999) 492–495.
- [41] S. Takayama, E. Ostuni, X. Qian, J. McDonald, X. Jiang, P. LeDuc, M.-H. Wu, D. Ingber, G. Whitesides, Topographical micropatterning of poly(dimethylsiloxane) using laminar flows of liquids in capillaries, *Advanced Matter* 13 (8) (2001) 570–574.
- [42] J. Sader, J. Chon, P. Mulvaney, Calibration of rectangular atomic force microscope cantilevers, *Review of Scientific Instruments* 70 (1999) 3967–3969.
- [43] C. White, R. Drzal, Viscoelastic characterization of polymers using dynamic instrumented indentation, *Mater. Res. Soc. Symp. Proc.* 841 (2005), R5.3.1–R5.3.6.
- [44] E. Oberg, F. Jones, H. Horton, H. Ryffell, *Machinery's Handbook*, 26th edition, Industrial Press Inc., 2000.
- [45] MatWeb, www.matweb.com.
- [46] G. Krishnan, C. Kim, S. Kota, Design synthesis of single point compliant mechanisms utilizing serial concatenation of building blocks, *Proceedings of the ASME International Design Engineering Technical Conference (IDETC)*, San Diego, CA.
- [47] D. Cappelleri, G. Krishnan, C. Kim, V. Kumar, S. Kota, Towards the design of a decoupled, two-dimensional, vision-based μ N force sensor, *ASME Journal of Mechanisms and Robotics* 2 (2010), 021010-1–021010-9.

Biographies

David J. Cappelleri is an assistant professor in the Department of Mechanical Engineering at Stevens Institute of Technology. His research interests include meso-, micro- and nano-scale robotics, manipulation and assembly, mechatronics, robotic system integration, medical robotics and device design, MEMS design and fabrication, and robotics and automation for the life sciences. He received his bachelor of mechanical engineering degree from Villanova University in 1998 and master of science in mechanical engineering degree from The Pennsylvania State University in 2000. He worked in the medical device industry on stereotactic radiosurgery, radiotherapy, and image-guided surgery products from 2000 to 2003 and then received his Ph.D. degree in mechanical engineering and applied mechanics from the University of Pennsylvania in 2008. He is a recipient of the Harvey N. Davis Distinguished Assistant Professor Teaching Award in 2010 and the Association for Lab Automation (ALA) Young Scientist Award for his paper at IEEE CASE 2009. He is an elected member of the IEEE Robotics and Automation Society Technical Committee on Micro/Nano Robotics and Automation, American Society of Mechanical Engineers (ASME) Design Engineering Division Mechanisms and Robotics Committee, and the ASME Design Engineering Division Micro and Nanosystems Technical Committee.

Gianluca Piazza is a Wilf Family Term Assistant Professor in the Department of Electrical and Systems Engineering (ESE) at the University of Pennsylvania. His research interests focus on piezoelectric micro and nano systems (MEMS/NEMS) for RF wireless communications, biological detection, wireless sensor platforms and all mechanical computing. He also has general interest in the areas of micro/nano fabrication techniques and integration of micro/nano devices with state-of-the-art electronics. He received his Ph.D. degree from the University of California, Berkeley in 2005. He has more than 10 years of experience working with piezoelectric materials. He holds two patents in the field of micromechanical resonators and has recently co-founded a start-up (Harmonic Devices Inc.) aiming at the commercialization of single-chip and multi-band RF filters and oscillators. He received the IBM Young Faculty Award in 2006 and has won, with his students, the Best Paper Award in Groups 1 and 2 at the IEEE Frequency Control Symposium in 2008 and 2009, respectively.

Vijay Kumar is the UPS Foundation professor and the associate dean for Academic Affairs in the School of Engineering and Applied Science at the University of Pennsylvania. He received his Ph.D. in mechanical engineering from The Ohio State University in 1987. He has been on the Faculty in the Department of Mechanical Engineering and Applied Mechanics with a secondary appointment in the Department of Computer and Information Science at the University of Pennsylvania since 1987. His research interests lie in the areas of robotics and manufacturing. He is a Fellow of the American Society of Mechanical Engineers (ASME) and the Institution of Electrical and Electronic Engineers (IEEE). He has served on the editorial boards of the *IEEE Transactions on Robotics and Automation*, *Journal of Franklin Institute*, *IEEE Transactions on Automation Science and Engineering*, *ASME Journal of Mechanical Design* and the *ASME Journal of Mechanisms and Robotics*. He is the recipient of the 1991 National Science Foundation Presidential Young Investigator award, the Lindback Award for Distinguished Teaching, the 1997 Freudenstein Award for significant accomplishments in mechanisms and robotics and the 2004 IEEE International Conference on Robotics and Automation Kawamori Best Paper Award. He is also a Distinguished Lecturer in the IEEE Robotics and Automation Society and an elected member of the Robotics and Automation Society Administrative Committee.